

Characteristics of two-azimuth seismic ionospheric disturbances following the 2020 Jamaica earthquake from GPS observations

Yi Chai¹ and Shuanggen Jin²

¹Shanghai Astronomical Observatory, Chinese Academy of Sciences

²Shanghai Astronomical Observatory, Chinese Academy of Sciences

November 21, 2022

Abstract

Earthquakes often occur and may induce the ionospheric disturbance. In order to understand the generation and process of the earthquake, the seismic ionospheric disturbance (SID) may provide insights on earthquakes. In this paper, the seismic ionospheric disturbances following the Mw 7.7 Jamaica earthquake on 28 January 2020 are detected after 12min of the main shock by the dual-frequency GPS measurements. Two disturbances in different azimuths are significantly found by satellite PRN26 and PRN03. The one is located at the southwest area in the range of 700-800km away from the epicenter while the other is located at the southeast area in the range of 200-450km. The propagation speeds of the two disturbances are 2.53km/s and 2.57km/s respectively. Furthermore, we estimated the detailed characteristics of SID (primarily the amplitude, elevation and azimuth angle, waveform and frequency) and discussed the generation and motion process of the ionospheric disturbance with seismograph, focal mechanism and magnetic field. The relation among SID, Rayleigh wave and focal mechanism are interpreted. Furthermore, the azimuthal asymmetry of SID amplitude and the appearance of the inverted N-shape waveform observed by satellite PRN26 are the main distinctions in the two disturbances as a result. Finally, the up propagating secondary acoustic wave triggered by the seismic Rayleigh wave from the strike-slip earthquake is the main source of the two disturbances.

1 Characteristics of two-azimuth seismic ionospheric
2 disturbances following the 2020 Jamaica earthquake
3 from GPS observations

4 Yi Chai ^{1,2}, Shuanggen Jin ^{1,3*}

5 ¹ Shanghai Astronomical Observatory, Chinese Academy of Sciences, Shanghai
6 200030, China

7 ² University of Chinese Academy of Sciences, Beijing 100047, China

8 ³ School of Remote Sensing and Geomatics Engineering, Nanjing University of
9 Information Science and Technology, Nanjing 210044, China

10

11 **Abstract:** Earthquakes often occur and may induce the ionospheric disturbance. In order to
12 understand the generation and process of the earthquake, the seismic ionospheric disturbance
13 (SID) may provide insights on earthquakes. In this paper, the seismic ionospheric
14 disturbances following the Mw 7.7 Jamaica earthquake on 28 January 2020 are detected after
15 12min of the main shock by the dual-frequency GPS measurements. Two disturbances in
16 different azimuths are significantly found by satellite PRN26 and PRN03. The one is located
17 at the southwest area in the range of 700-800km away from the epicenter while the other is
18 located at the southeast area in the range of 200-450km. The propagation speeds of the two
19 disturbances are 2.53km/s and 2.57km/s respectively. Furthermore, we estimated the detailed
20 characteristics of SID (primarily the amplitude, elevation and azimuth angle, waveform and
21 frequency) and discussed the generation and motion process of the ionospheric disturbance
22 with seismograph, focal mechanism and magnetic field. The relation among SID, Rayleigh
23 wave and focal mechanism are interpreted. Furthermore, the azimuthal asymmetry of SID
24 amplitude and the appearance of the inverted N-shape waveform observed by satellite
25 PRN26 are the main distinctions in the two disturbances as a result. Finally, the up
26 propagating secondary acoustic wave triggered by the seismic Rayleigh wave from the
27 strike-slip earthquake is the main source of the two disturbances.

28 **Keywords:** seismic ionospheric disturbance (SID); GPS; Rayleigh wave; strike-slip earthquake

29

30 **1. Introduction**

31 Earthquakes are common natural disasters. During the main shock of an earthquake, the
32 earthquake rupture and severe co-seismic vertical crust movements can excite acoustic
33 resonance, and some of the acoustic resonance can propagate upward into the ionosphere in

34 the form of acoustic waves and induce variations of the ionospheric electron density which is
35 the so-called ionospheric disturbances. In short, the ionospheric disturbances relate to the
36 acoustic-gravity wave launched by big earthquake [1,2]. The first ionosphere disturbance was
37 detected by ionospheric vertical sounding following the great Alaska earthquake in 1964 [3].
38 And the frequency oscillations in radio signals follow the Alaska were detected in the same
39 earthquake [4]. Since then, the researches for seismic ionospheric disturbance (SID) have
40 attracted great attention and made contributions to reveal the mechanism of earthquake
41 motion and crust vertical movement.

42 However, as the limitation of the measurement instruments in last few decades, there are
43 difficulties in studying the more detailed characteristics of ionospheric disturbance.
44 Nowadays, dense Global Position System (GPS) networks has been a new method to detect
45 seismic ionospheric disturbance since 1990s [5] and it has strong imaging capability, high
46 spatial resolution and sensibility for detecting Rayleigh wave in the ionosphere [6]. With the
47 widely use of GPS, the properties of SID and the relationship among seismic ionospheric
48 disturbance, earthquake and ionosphere will be better understood. By estimating the
49 ionospheric delays of GPS [7], the total electron content (TEC) can be precisely calculated so
50 that the seismic ionospheric anomaly signal which contain the source information related to
51 the earthquake can be detectable from the GPS-TEC time series observation[8]. It will provide
52 a chance to drive the complete process and the properties of the earthquake, after modeling
53 the SID signal. On the other hand, as the short time for SID signal reach to the ionosphere
54 (around 8 minutes), it will have potential in the near-real-time earthquake monitoring and
55 real-time tsunami warning [9], by modeling and estimating of SID.

56 Hitherto, many studies for seismic ionospheric disturbance by using dense GPS
57 measurement have been conducted. For example, Afraimovich et al. (2010) found the
58 intensive N-shaped shock-acoustic waves with a plane waveform following the 2008
59 Wenchuan earthquake [10]. The ionospheric disturbance following the 2015 Mw 7.8 Nepal
60 Earthquake is detected by GPS-TEC and it is caused by the acoustic gravity wave induced by
61 Rayleigh wave [11]. Zhou et al. (2017) found the large-scale ionospheric anomalies near the
62 epicenter two days prior to the same 2015 Mw 7.8 Nepal Earthquake from GPS observations
63 of the Crustal Movement Observation Network of China (CMONOC) [12]. Another seismic
64 ionospheric perturbation following the Mw 9.0 Tohoku Earthquake in Japan was found from
65 nationwide GPS receiving networks and the disturbance was confirmed existing three
66 different propagation velocities [13,14,15].

67 Although numerous previous studies have detected and estimated the seismic
68 ionospheric disturbance, there are still problems and difficulties in studying seismic
69 ionospheric disturbance. For instance, the distinct TEC anomaly can be detected by GPS
70 measurement only for earthquakes with large magnitudes ($M_w > 6.8$) [16], as the larger vertical
71 crustal displacement or deformation cause significant CID. And the uneven distribution of
72 ground-base GPS network makes the absence of ionospheric disturbance in some seismic
73 regions. Besides, it is difficult to conclude the generation mechanism of CID in a simple
74 theory, for the characteristics of CID, such as amplitude, propagation speed, period, azimuth
75 angle, phase and waveform, vary with the factors of the earthquakes, for example, magnitude
76 and focal mechanism[17,18] ; the pattern of rupture and ground deformation [10, 17]; the

77 geomagnetic field [9, 17] and geometry of GPS-sounding [19]. Consequently, abundant
78 investigations of different earthquake event are necessary.

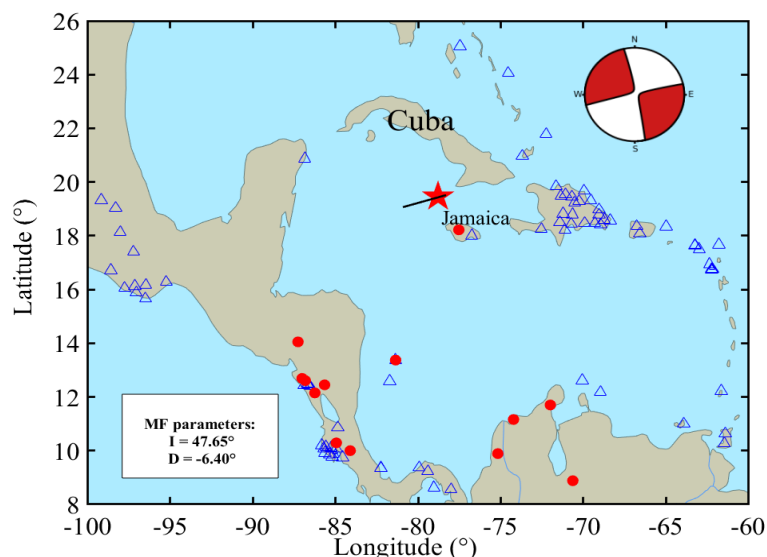
79 2. Data and Method

80 2.1. Earthquake information

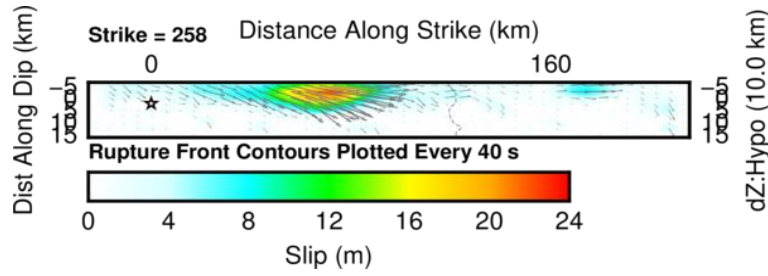
81 The 2020 M_w 7.7 earthquake ($19.46^\circ\text{N}, 78.79^\circ\text{W}$) occurred in the Caribbean Sea to the
82 south of Cuba and northwest of Jamaica, with 10km in depth at 19:10:22(UTC), 28 January
83 2020, which is the result of the strike-slip faulting on the plate boundary between the North
84 America and Caribbean tectonic plates. The epicenter is located at the plate boundary and the
85 fault plane strikes along with the orientation of the plate boundary. The GPS observation data
86 with a sampling rate of 15s was obtained from dense GPS stations conducted by University
87 Navstar Consortium (UNAVCO).

88 The distribution of 93 GPS stations and 13 seismographs are shown in Figure 1 with the
89 blue triangles and red filled circles. The data of seismometers is provided by IRIS. The red
90 pentagram represents the epicenter of the 2020 M_w 7.7 earthquake and black line represents
91 the fault plane near the epicenter. The beach ball indicates the focal mechanism of the
92 earthquake event at the upper-right corner of the figure. Magnetic field (MF) parameters
93 involving inclination (I) and declination (D) are shown in the white panel at lower left quarter.
94 The slip distribution map of the 2020 M_w 7.7 Jamaica earthquake is shown in Figure 1(b).
95 Related information (finite fault and slip distribution) of this earthquake event is accessible
96 form U.S. Geological survey (USGS). The slip distribution map indicates the motion direction
97 of fault plane in strike of 258° with arrows and slip amplitude in color.

(a) Map of seismic area



(b) Slip distribution map



99

100 **Figure 1.** The Mw 7.7 Jamaica earthquake event. (a) Distribution of GPS stations and
 101 seismographs around the epicenter area and basic information about the earthquake. (b) The
 102 slip distribution map from USGS (<https://earthquake.usgs.gov>).

103 2.2. Method

104 The ionosphere disturbances can be extracted from GPS-TEC time series. During the
 105 propagation of GPS satellite signals, the ionosphere delay in signals relates to the GPS signal
 106 frequency and ionosphere TEC. Therefore, in order to get the ionosphere disturbances, the
 107 ionosphere TEC should be calculated precisely from the dual-frequency GPS observation ($f_1 =$
 108 1,575.42 MHz, $f_2 = 1,227.60$ MHz) by the following equation [20,21]:

$$109 \quad STEC = \frac{f_1^2 f_2^2}{40.3(f_1^2 - f_2^2)} (L_1 - L_2 + \lambda_1(N_1 + b_1) - \lambda_2(N_2 + b_2) + \varepsilon_L)$$

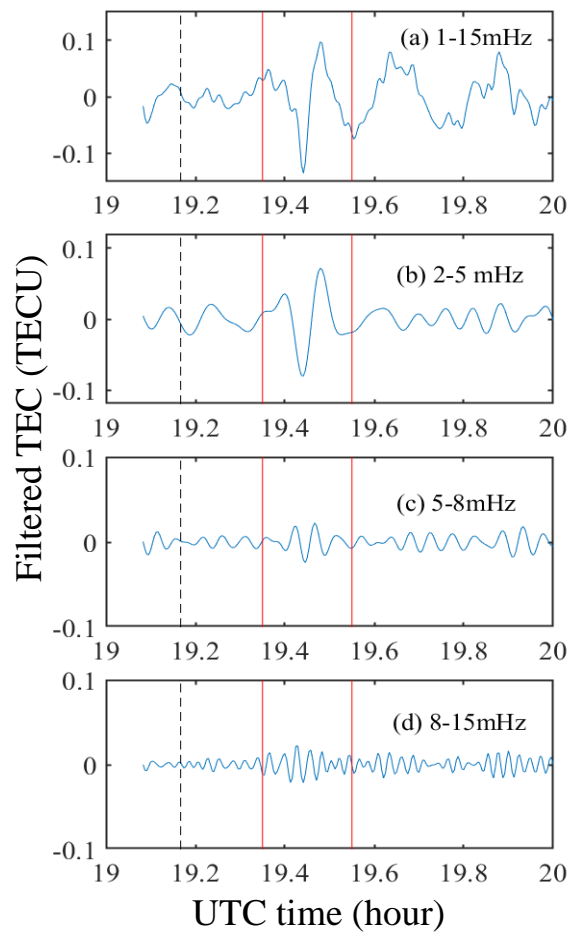
$$STEC = \frac{f_1^2 f_2^2}{40.3(f_1^2 - f_2^2)} (P_1 - P_2 - (d_1 - d_2) + \varepsilon_p)$$

110 Where STEC is slant total electron content, L_1 and L_2 are the GPS carrier phase
 111 measurements, P_1 and P_2 are the GPS code measurements, λ_1 and λ_2 are the GPS signal
 112 wavelength, N is the ambiguity, b is the instrument biases for carrier phase, d_1 and d_2 are the
 113 differential code biases, and ε is the residual. STEC represents the absolute magnitude of
 114 ionosphere TEC. In order to get the relative variation of the ionosphere TEC and estimate the
 115 characters of seismo-ionospheric disturbances, the STEC along the GPS line of sight (LOS) is
 116 required to be vertical TEC(VTEC) converted by the following mapping function:

$$117 \quad VTEC = STEC * \cos \left[\arcsin \left(\frac{R \sin(z)}{R + H} \right) \right]$$

118 Where H is the height of the ionosphere shell, in this article, H is assumed at 350km of
 119 altitude. R is the earth's radius, and z is the elevation of the satellite. The calculated VTEC is
 120 used in forming GPS-TEC time series. However, cycle slip is the main error in obtaining
 121 high-precision TEC values from above method [22]. Therefore, the second-order
 122 time-difference phase ionospheric residual (STPIR) was used to eliminate cycle slip in this
 123 article [23]. Besides, the background noise of ionosphere and TEC variation should be taken
 124 into consideration in order to get the precise GPS-TEC time series. In this article, the

125 Butterworth filter of a fourth-order zero-phase finite impulse was used to remove the
126 background noise and obtain the filtered TEC series, which related to the earthquake.
127 According to the Nyquist sampling theory, the Nyquist frequency is about 8mHz for GPS
128 observation which sampling interval is 60s. In this article, the sampling interval of GPS
129 observation data is 15s, thus the Nyquist frequency is larger than 8mHz. As 2mHz is the
130 cutoff frequency of acoustic above the ionospheric height. The GPS-TEC time series obtained
131 from station LMNL and satellite PRN26 with different passband frequency are shown in
132 Figure 2. As shown in Figure 2, the distinct seismo-ionospheric disturbance can be found out
133 from the series with the 2-5mHz passband frequency about 12 min after the occurrence of the
134 earthquake in the red lines marked zone, so the fourth-order zero-phase Butterworth filter
135 with passband frequency of 2 and 5mHz was used to obtain the GPS-TEC time series.



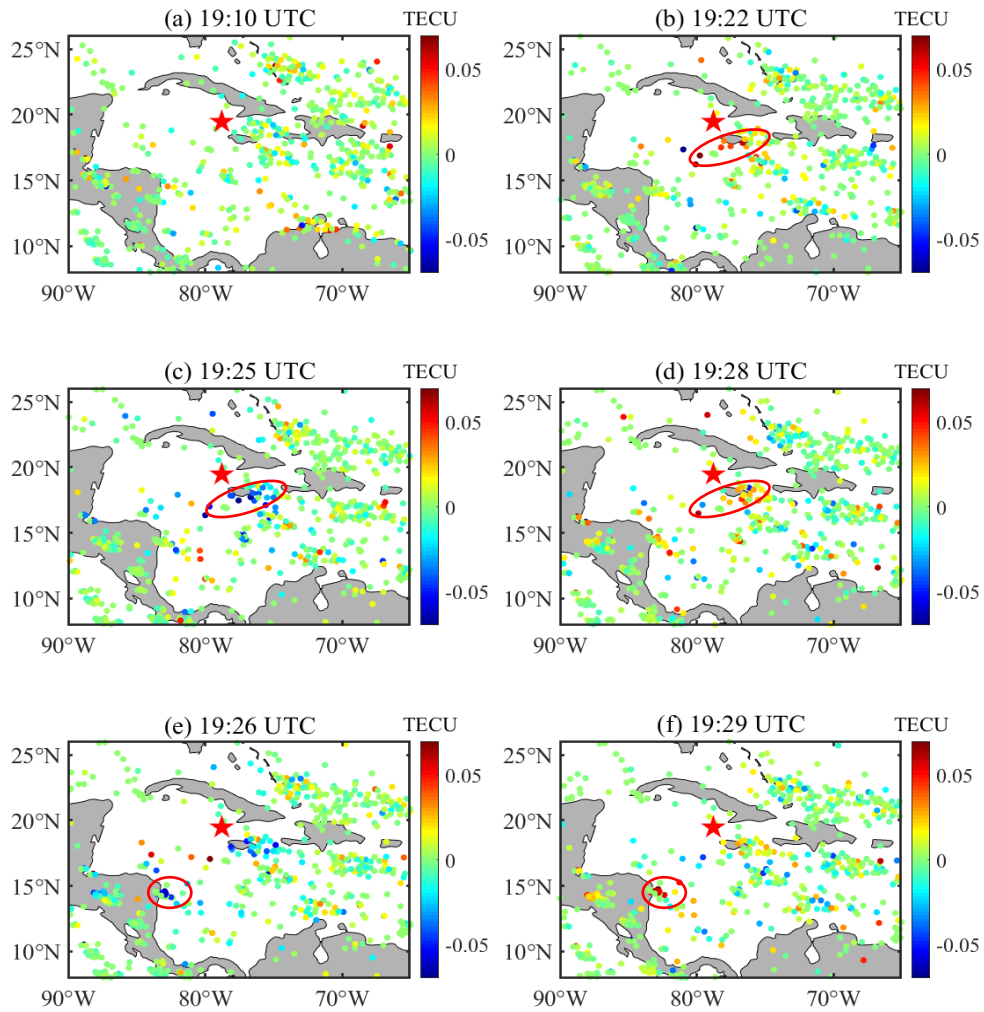
136

137 **Figure 2.** GPS-TEC time series observed by station LMNL and satellite PRN26 with different
138 filter passband frequency. (a) TEC series with 1-15mHz passband. (b) TEC series with 2-5mHz
139 passband. (c) TEC series with 5-8mHz passband (d) TEC series with 8-15mHz passband. The
140 dashed black line represents the eruption time of the 2020 Jamaica earthquake.

141 3. Results and discussion

142 3.1. Co-seismic ionospheric disturbances

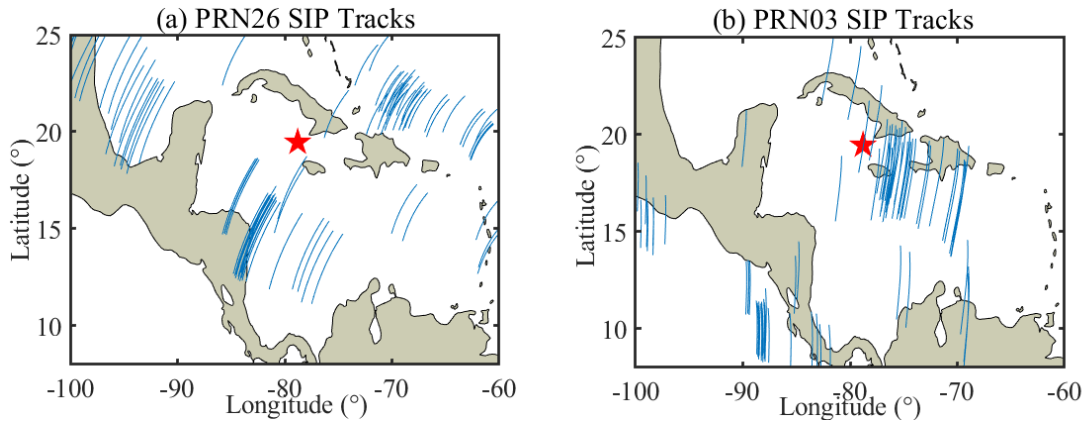
143 By using the GPS measurement, the TEC responses and co-seismic ionospheric
144 disturbances following the 2020 Jamaica earthquake are detected and estimated. Figure 3
145 shows the TEC distribution maps from 19:10 UTC to 19:30 UTC. The red pentagram
146 represents the epicenter and the colorful filled dot is corresponding to the subionospheric
147 point (SIP) and the positions of these dots represent the locations of SIPs. The color values
148 show the variation amplitude of filtered TEC and the color bar indicates the variational value
149 range of filtered TEC series (in TECU). As is shown Figure 3, the 2020 Jamaica earthquake
150 occurred at 19:10 UTC. However, there are no obvious ionospheric anomalies at first (Figure
151 3a). After about 12 min of the main shock, significant ionospheric anomalies are first detected
152 at the southeast region of epicenter (200-450km away from the epicenter). Most of the TEC
153 disturbances display in positive anomalies (Figure 3b). The average variation amplitude of
154 these TEC disturbances reaches to 0.05 TECU ($1 \text{ TECU} = 10^{16} \text{ e/m}^2$). Around 3min later at 19:25
155 UTC, the TEC disturbances become stronger and the variation amplitude reaches its
156 maximum which is about 0.07TECU at this time. It should be noticed that the TEC
157 disturbances turn positive anomalies to negative anomalies (Figure 3c). The negative TEC
158 anomalies last for around 3min and turn back to positive anomalies in the same area at 19:28
159 UTC (Figure 3d). The amplitude of TEC disturbances begins to deplete, which is about
160 0.04TECU. Besides, another significant ionospheric anomaly is detected at the southwest area
161 around 700-800km away from the epicenter at 19:26 TECU (Figure 3e).. The TEC disturbances
162 have a larger variation amplitude which reaches to 0.07 TECU. After the same time interval as
163 the previous discussed TEC disturbance (3 min), the TEC disturbances show an opposite
164 polarity change (Figure 3f) at 19:29UTC. After 19:30 UTC, no obvious TEC disturbances can
165 be detected. Based on above preliminary estimate, two TEC disturbances exist in different
166 azimuth of the seismic region.



167

168 **Figure 3.** Filtered TEC distribution maps during 19:10-19:30 UTC. The red pentagram
 169 represents the location of the epicenter and the color filled dots indicate the positions of SIPs.
 170 The color bar is the variational value range of filtered TEC.

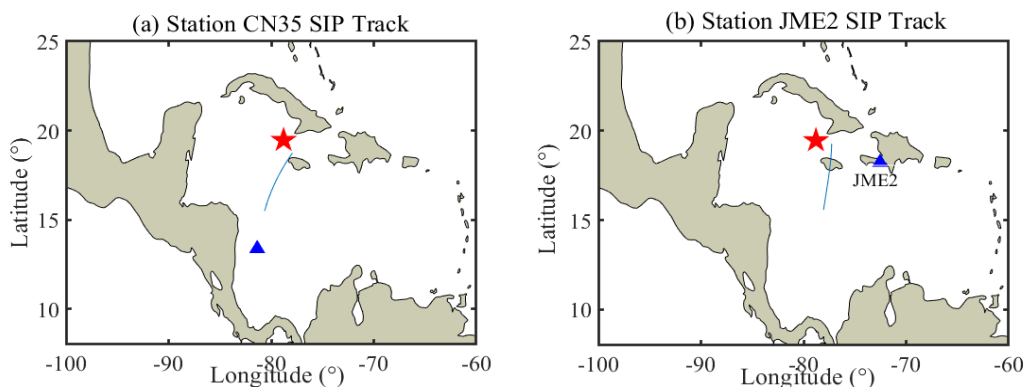
171 In order to comprehend the relationship between earthquake and seismic ionospheric
 172 disturbance, the further specific characteristics of the TEC disturbances should be estimated.
 173 Figure 4 shows the SIP tracks between the satellites and the stations at the height of 350km
 174 during 18:45-20:00 UTC. It can be seen that the SIP tracks obtained from the two satellites
 175 cover the most area around south of the epicenter. The SIP tracks of PRN03 mainly cover the
 176 southeast area of the epicenter while the PRN26's mainly cover the northwest, southwest and
 177 northeast area.



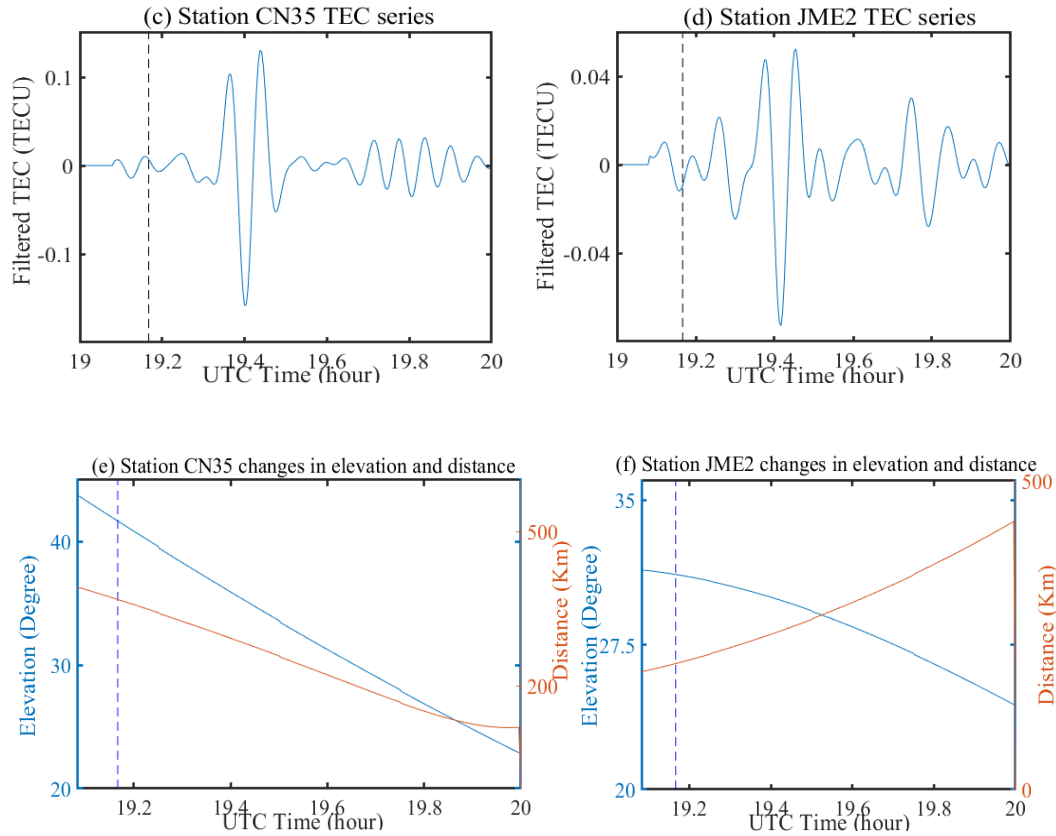
178

179 **Figure 4.** The SIP tracks between the satellites and the stations. (a) The SIP tracks with PRN26.
 180 (b) The SIP tracks with PRN03.

181 Figure 5 shows more detailed characters about these two TEC disturbances. It shows the
 182 SIP tracks of station CN35 with PRN26 (Figure 5a) and station JME2 with PRN03 (Figure 5b)
 183 during 19:05-20:00 UTC, corresponding filtered GPS-TEC time series and the changes in the
 184 satellite elevation angle and distance. The two graphs on the left displays the SIP tracks, the
 185 red pentagram represents the location of epicenter, the blue triangles represent the location of
 186 station CN35 and JME2. Both SIP tracks locate in the near-field of the epicenter. The middle
 187 two displays the GPS-TEC time series in typical N-shaped waveform observed by station
 188 CN35 with PRN26 and station JME2 with PRN03. The dashed line indicates the eruption time
 189 of the 2020 Jamaica earthquake. The distinct ionosphere disturbance can be observed clearly
 190 after about 12min of the main shock from both series. The difference is that the negative
 191 variation amplitude of the series observed by station CN35 with PRN26 reaches more than
 192 0.15 TECU, while the negative variation amplitude of station JME2 with PRN03 reaches only
 193 to 0.07 TECU. The changes in the satellite elevation angle (in blue line) and distance (in
 194 orange line) are shown in the right two graphs. The satellite elevation angle between station
 195 CN35 and satellite PRN26 decreases from 40° to 22° , while the satellite elevation angle
 196 between station JME2 and satellite PRN03 decreases from 31° to 25° . These two elevation
 197 angles both belong to low elevation angle range, which is sensitive to the detection of
 198 co-seismic ionospheric disturbances caused by big earthquakes [24].



199



200

201

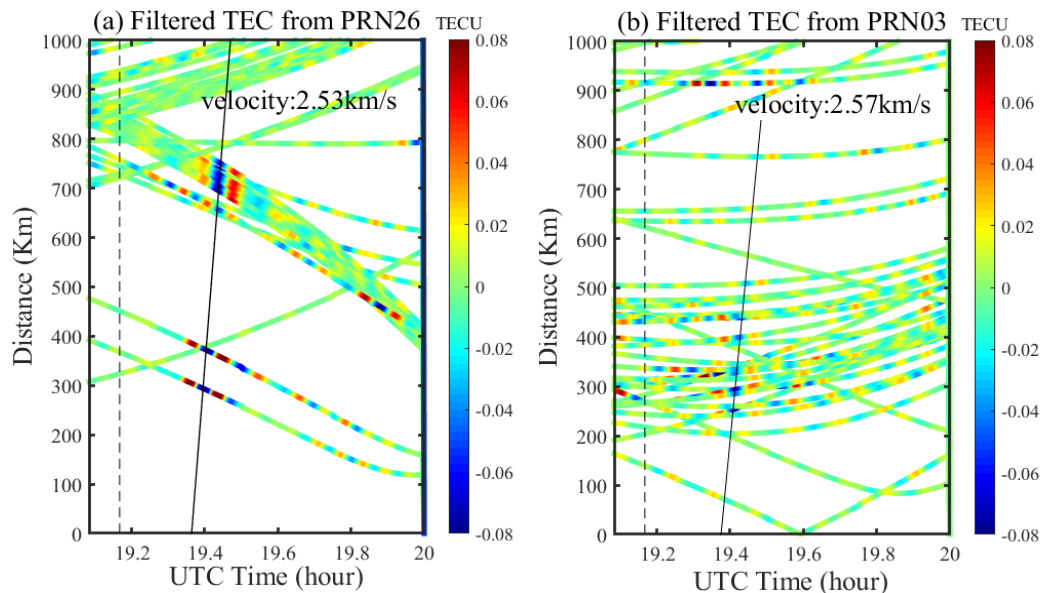
202 **Figure 5.** (a) SIP track observed by station CN35 with satellite PRN26. (b) SIP track observed
 203 by station JME2 with satellite PRN03. (c) TEC series from station CN35, PRN26 observation.
 204 (d) TEC series from station JME2, PRN03 observation. (e) Changes in elevation and distance
 205 of station CN35,PRN26. (f) Changes in elevation and distance of station JME2,PRN03.

206 *3.2. Two-azimuth disturbances*

207 The earthquakes may excite a variety of different co-seismic ionospheric
 208 disturbances. For example, the two-mode ionospheric disturbances are detected and
 209 estimated following the 2005 Northern California offshore earthquake [24]. And
 210 Astafyeva et al. (2009) found another two-mode long-distance co-seismic ionospheric
 211 disturbance following the great 1994 Kurile earthquake [25]. The research for
 212 propagation characters of ionospheric disturbances can demonstrate the pattern, modes,
 213 generation mechanism and source of co-seismic ionospheric disturbances. In section 3.1,
 214 we have found two ionospheric disturbances in different azimuth. In this section, the
 215 generation source and further characteristics of the two disturbances are estimated and
 216 discussed. Figure 6 shows the traveling-time diagrams of filtered GPS-TEC time series
 217 from satellites PRN26 and PRN03. These two diagrams demonstrate the linear
 218 relationships between the seismic ionospheric disturbance travel time and distance from
 219 SIP to the epicenter. The color of the curves indicates the variation value of filtered TEC
 220 series. Two significant ionospheric disturbances can be found through the traveling-time
 221 diagrams. After performing the linear fit, the propagation velocity of the ionospheric
 222 disturbances detected by PRN26 is about 2.53km/s while the PRN03's is around 2.57km/s.

223 The ionospheric disturbance generated by different sources can be distinguished through
 224 the velocity of their propagation. These two velocities are larger than sound speed at the
 225 ionospheric altitude (~1km/s) but lower than the Rayleigh surface wave propagation
 226 speed which propagates along the ground surface with velocity 3000-4000m/s [26].
 227 According to Jin (2018), the two ionospheric disturbances are probably both the
 228 secondary acoustic wave generated by seismic Rayleigh waves with dynamic coupling
 229 [24].

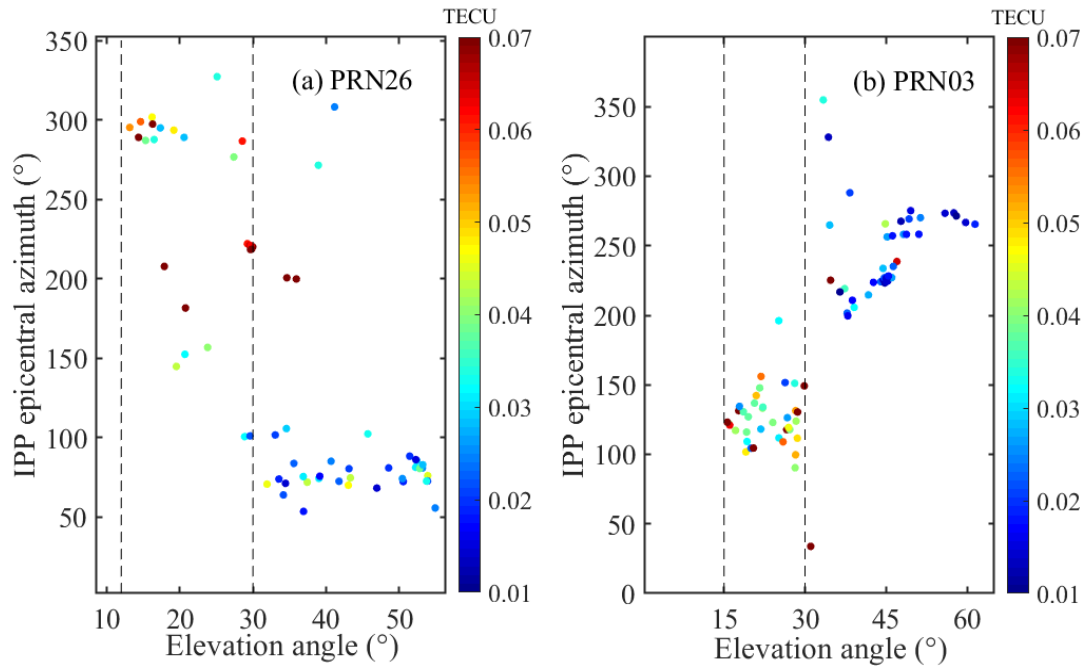
230 In the left diagram, the disturbance is detected by PRN26 after 12 min of the main
 231 shock in 300- 800km away from the epicenter. The amplitude of the negative polarity is
 232 larger than 0.08 TECU. On the other hand, the disturbance detected by PRN03 at the
 233 same time in 250-500km away from the epicenter has a lower negative amplitude which
 234 only reaches to 0.05 TECU. Therefore, the two disturbances have different amplitude
 235 characteristics.



236

237 **Figure 6.** Traveling-time diagrams of seismic ionospheric disturbances from PRN26 (a) and
 238 PRN03 (b). The dashed black line represents the eruption time of the 2020 Jamaica earthquake.
 239 The color bars indicate the value range of filtered TEC series. The black diagonal line is used
 240 to linear fit the propagation velocity of TEC disturbances.

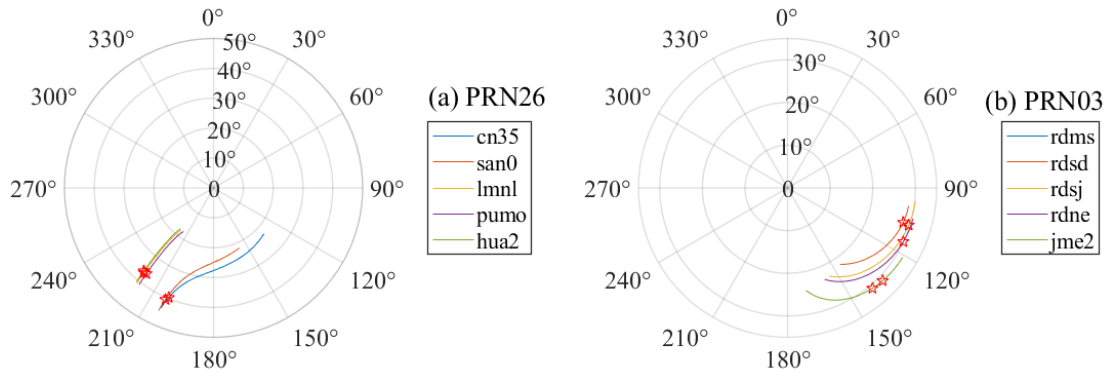
241 Figure 7 shows the distribution of IPP epicentral azimuth and elevation angle of the
 242 maximum in each GPS-TEC time series. The color of dot indicates the value of the maximum.
 243 As is shown in the left scatter diagram (Figure 7a), the dots which larger than 0.03 TECU are
 244 mainly at the elevation angles 12-30° of corresponding line of sight (LOS). The dots are
 245 mainly at elevation angles 15-30° of corresponding LOS in the right scatter diagram (Figure
 246 7b). The distribution of the GPS elevation angle contributes to distinguish the horizontal and
 247 vertical disturbance acoustic wave propagations. The elevation angles corresponding to the
 248 maximum in each GPS-TEC time series with PRN26 and PRN03 are both in the range of low
 249 elevation angles. Therefore, the two ionospheric disturbances both propagate along vertical
 250 direction to the ionosphere.



251

252 **Figure 7.** (a) Distribution of IPP epicentral azimuth and elevation angle of the maximum in
 253 filtered TEC series observed from PRN26. (b) Distribution of IPP epicentral azimuth and
 254 elevation angle of the maximum in filtered TEC series observed from PRN03. The
 255 maximum filtered TEC less than 0.01 TECU are neglected.

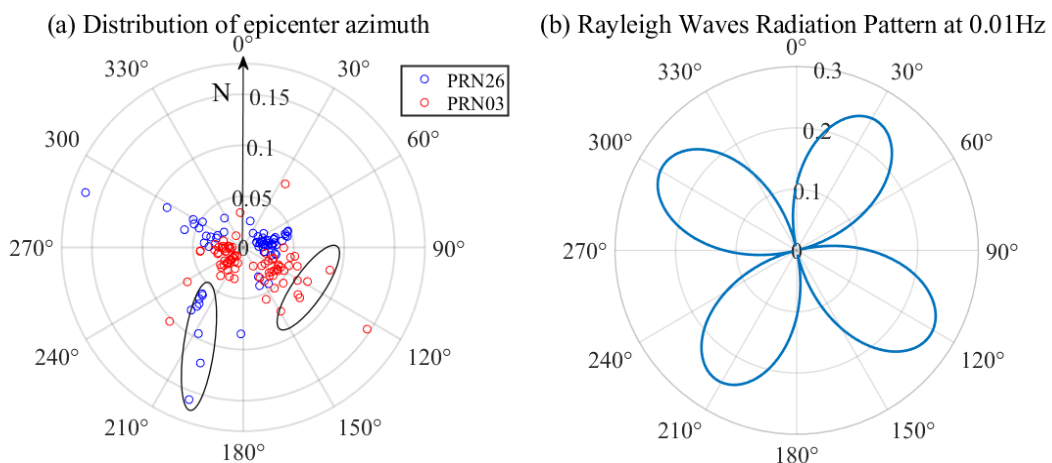
256 Figure 8 shows the change curves in the elevation angles and SIP epicenter azimuth of
 257 the stations which have detected the ionospheric disturbances in the form of polar diagram
 258 from 19:00-20:00 UTC. The theta axis represents the SIP epicentral azimuth (in degree). The
 259 radius axis represents the elevation angles (in degree). The red pentagram represents the
 260 corresponding elevation angle and epicenter azimuth at the eruption time of the earthquake.
 261 It can be clearly seen from the curves that all the elevation angles are low angles and the
 262 values of angle are decreasing since the eruption time of earthquake. According to previous
 263 work [26], lower elevation angle can enlarge the horizontal extent of the ionospheric region.
 264 When the disturbance wave vector is perpendicular to satellite-to-receiver line of sight (LOS),
 265 the observed amplitude reaches to largest amount. On the other hand, the amplitude of the
 266 disturbance signal is relevant to the satellite elevation angle. However, with the combination
 267 of Figure 7 and Figure 8, the elevation angles of the IPP or SIP observed by PRN03 and
 268 PRN26 are both at the low angle range. Besides, the consistent trend in the change of
 269 elevation angle can be clearly found. Thus, ionospheric disturbance can be detected more
 270 easily at low satellite elevation angle.



271

272 **Figure 8.** The polar diagram of the changes in the elevation angles and SIP epicenter azimuth
 273 of selected stations with satellite PRN26(a) and PRN03(b) during 19:00-20:00 UTC.

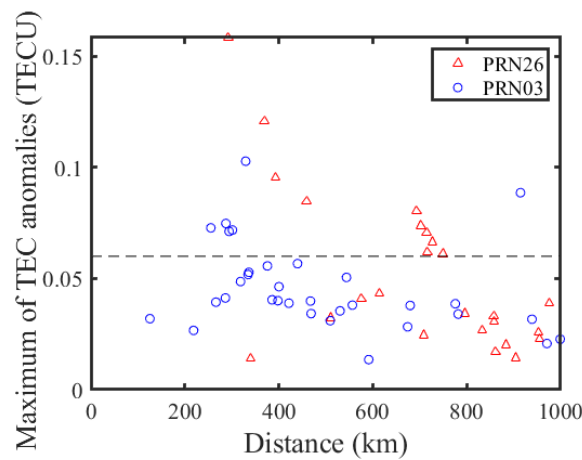
274 Figure 9(a) shows the distribution of the SIP epicenter azimuth for the maximum of each
 275 GPS-TEC time series in the form of polar diagram. The theta axis represents the SIP epicenter
 276 azimuth (in degree). The radius axis represents the variation value of the filtered TEC (in
 277 TECU). The north direction is set as the 0° azimuth. The red hollow dot represents the
 278 maximum of TEC series obtained from PRN03 and the blue hollow dot represent the
 279 maximum of TEC series observed by PRN26. The maximums of TEC series detected by
 280 PRN26 which are larger than 0.05 TECU mainly locate around epicenter azimuth 210°, while
 281 the maximums of TEC series obtained from PRN03 which are larger than 0.05 TECU mainly
 282 locate at epicenter azimuth 120-150°. This confirms that two different ionospheric
 283 disturbances exist in southwest and southeast area respectively combined with the result of
 284 TEC distribution maps in Figure 3(c) and (e). Figure 9(b) is Rayleigh waves radiation pattern
 285 at 0.01Hz frequency graph. The theta axis represents the azimuth (in degree) and the radius
 286 axis represents the amplitude of Rayleigh waves at 0.01Hz (in m/Hz). Relevant azimuth and
 287 amplitude data is downloaded from IRIS. Radiation pattern graph describe the amplitude
 288 component of Rayleigh waves in all directions. The amplitude of Rayleigh waves at 0.01 Hz
 289 reaches peak value in direction of azimuth 120° and 210°, which is consistent with the
 290 azimuth distribution of the two ionospheric disturbances. It indicates that the Rayleigh waves
 291 propagating along southwest direction (around azimuth 210°) and southeast direction
 292 (around azimuth 120°) have a large vertical displacement amplitude to induce the co-seismic
 293 ionospheric disturbance.



294

295 **Figure 9.** (a) The polar diagram of the distribution of the SIP epicenter azimuth for the
296 maximum of each GPS-TEC time series. (b) Rayleigh waves radiation pattern diagram at
297 0.01Hz frequency.

298 Figure 10 shows the distance distribution of the maximum in each TEC series for the
299 ionospheric disturbances detected by satellite PRN26 and PRN03. The red triangles represent
300 the maximum amplitude of TEC series observed by PRN26 and the blue circles represent the
301 TEC series observed by PRN03. The TEC series obtained by PRN03 have the maximum
302 amplitude lower than 0.06 TECU in the range of 200-450km away from the epicenter, while
303 PRN26 detect larger amplitude TEC disturbances which are larger than 0.06 TECU in
304 300-800km away from the epicenter. Therefore, combined with the TEC distribution maps
305 shown in Figure 3, the two disturbances detected by PRN26 and PRN03 respectively differ in
306 amplitude and distance distribution characteristic.



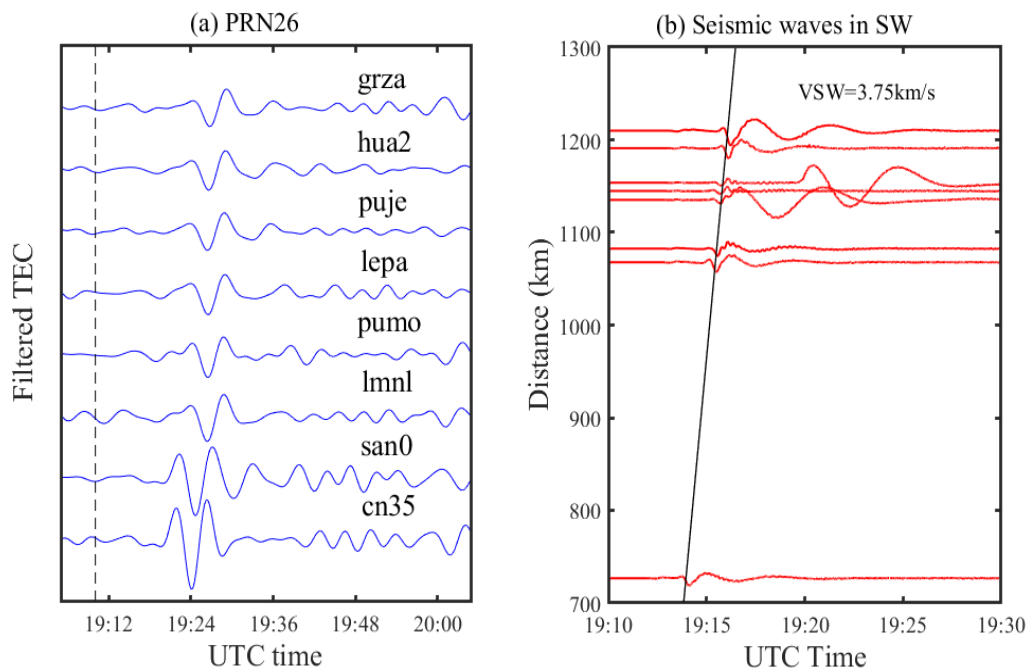
307

308 **Figure 10.** distance distribution of the maximum of each TEC series for the ionospheric
309 disturbances detected by satellite PRN26 and PRN03. The red triangles represent the TEC
310 series observed by PRN26 and the blue circles represent the TEC series observed by PRN03.

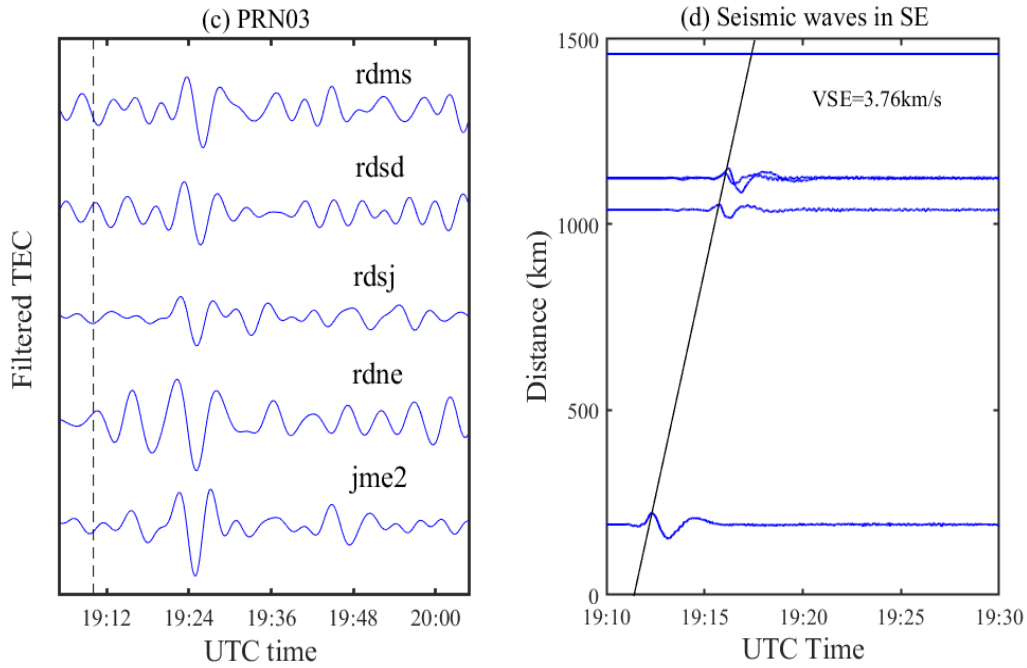
311 3.3. CID waveform and spectrum signature

312 Analysis for disturbances signal waveform and spectrum can provide more information
313 about characteristics of the two-azimuth ionospheric disturbances to distinguish their
314 differences . Figure 11 shows some cases of disturbances signal waveforms and seismic
315 waveforms in southwest and southeast direction. Disturbance waveforms observed by PRN26
316 are shown in Figure 11(a), while disturbance waveform observed by PRN03 are displayed in
317 Figure 11(c). The x-axis represents the UTC time. The dashed black line represents the
318 eruption time of the earthquake, the name of selected station is located in the right side of
319 each corresponding waveform. The significant TEC disturbances can be distinguished from
320 the waveforms after about 12 min of the main shock, which is in consistent with the results of
321 TEC distribution map shown in Figure 3 and traveling-time diagrams of seismic ionospheric
322 disturbances shown in Figure 6. As the distance between selected station and epicenter
323 increases, the amplitude of waveforms become to decrease, and the appearance time of
324 ionospheric disturbances begin to delay. It is noticeable that, in Figure 11(a), the signals
325 observed by station CN35 and SAN0 show a typical N-shape waveform. However, as the

326 distance from epicenter increases, the waveforms observed by far-field station LMNL, PUMO,
 327 LEPA, PUJE, HUA2 and GRZA appear in the form of an inverted N-shaped waveform
 328 (negative half-phase appear first [27]). In Figure 11(c), all the waveforms have N type forms,
 329 which is different from the waveforms of selected stations with PRN26. The detection of
 330 inverted N-shape and N-shape waveform indicates polarity divergence in the two-azimuth
 331 ionospheric disturbances. With the same passband filtering, the seismic waveforms at
 332 2-5mHz in southwest and southeast direction from the vertical broadband high-gain
 333 seismometers are shown in Figure 11(b) and (d) respectively. The y-axis represents the
 334 distance between seismograph and epicenter. And the x-axis indicates UTC time. Through
 335 liner fitting, the group speed of seismic waves in southwest direction is about 3.75km/s,
 336 which is close to the speed 3.76km/s in southeast direction. These two propagation speed are
 337 both in the velocity range of Rayleigh surface wave. Besides, it should be noticed that the
 338 seismic waves in SW show a negative polarity, which is consistent with the inverted N-shape
 339 waveform of Rayleigh wave-induced ionospheric disturbance observed by PRN26 in the
 340 southwest area. The same result can be concluded by comparing Figure 11(c) and (d). It is
 341 believed that the polarity of co-seismic ionospheric disturbance is determined by the polarity
 342 of generation source wave.



343

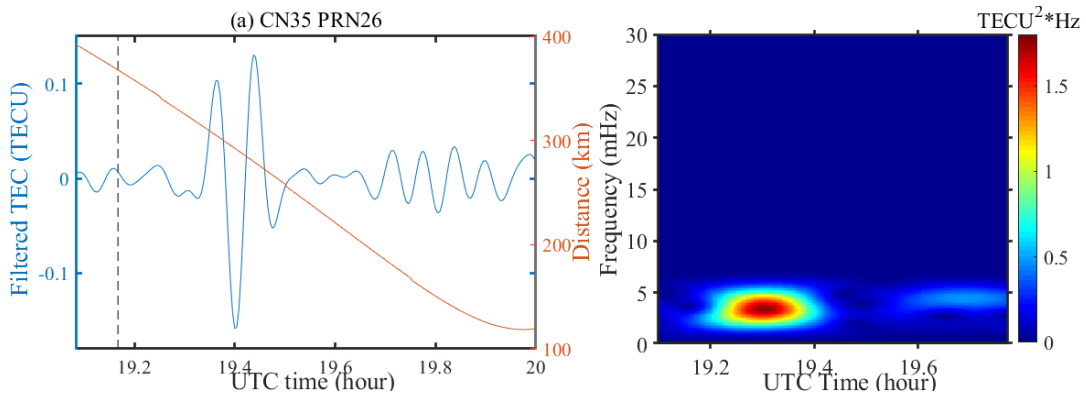


344

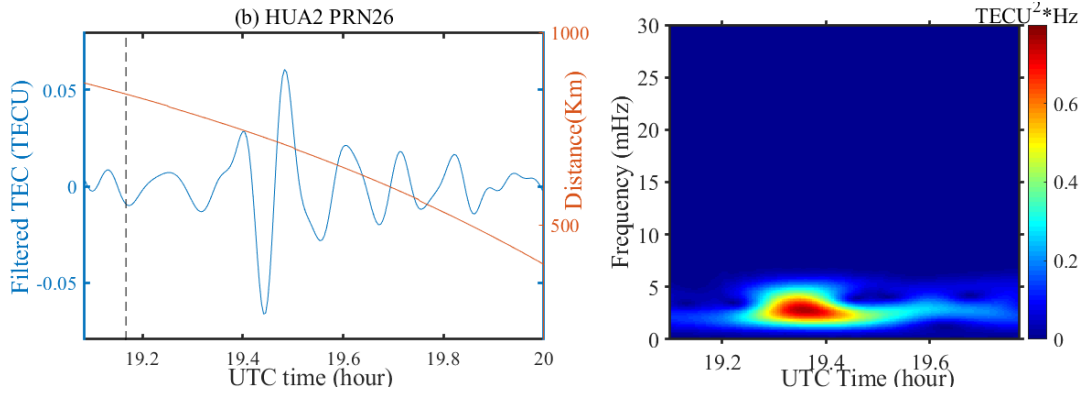
345

346 **Figure 11.** (a) Disturbance waveforms from observation of selected stations in PRN26. (b)
 347 Seismic waves in southwest direction (c). disturbance waveforms from observation of selected
 348 stations in PRN03. (d) Seismic waves in southeast direction.

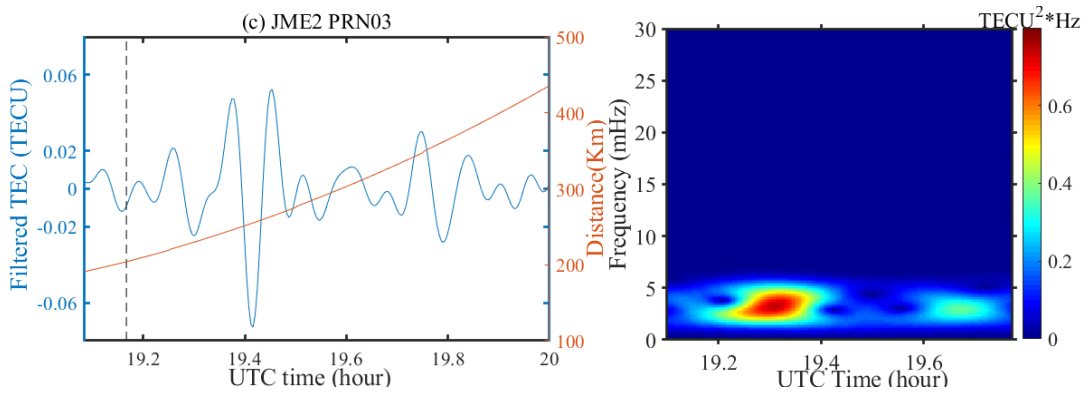
349 Furthermore, Figure 12 shows the spectrograms of TEC disturbance series from selected
 350 stations and satellites after using short-time Fourier transform (STFT) to convert TEC series
 351 from time domain to the frequency domain. The diagram order is station CN35 for PRN26,
 352 station HUA2 for PRN26, station JME2 for PRN03 and station RDMS for PRN03 respectively.
 353 The left panel displays the TEC time series in blue line and distance changes in orange line,
 354 and the right panel represents the spectrogram of corresponding TEC time series converting
 355 from STFT. The center frequency of disturbance signals for station CN35 and station GRZA is
 356 about 3.4mHz and 3mHz, while frequency of disturbance signals for station JME2 and station
 357 RDMS is centered at about 3.3mHz and 3.1mHz. The center frequencies for selected stations
 358 are all in the frequency range of infrasonic wave. Therefore, the two ionospheric disturbances
 359 detected by PRN26 and PRN03 show a same frequency characteristic..



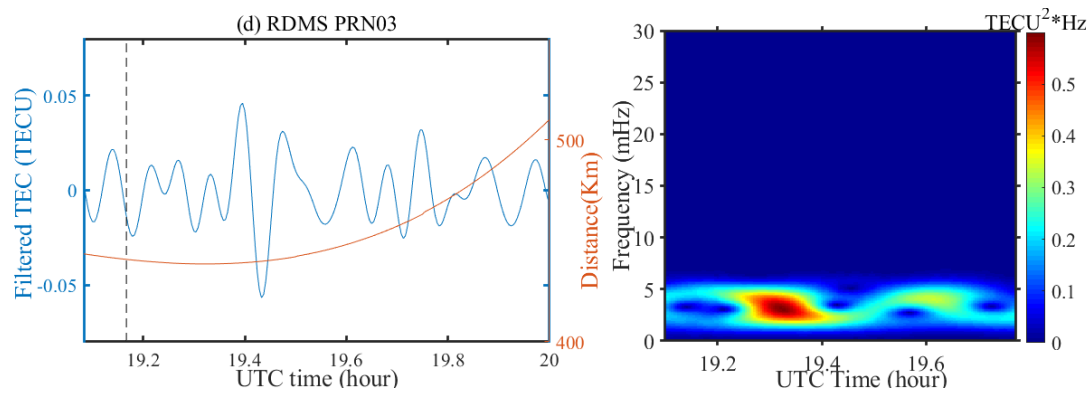
360



361



362



363

364 **Figure 12.** The spectrograms of TEC disturbances series from selected stations and satellites.
 365 (a) Station CN35 of satellite PRN26. (b) Station GRZA of satellite PRN26. (c) Station JME2 of
 366 satellite PRN03. (d) Station RDMS of satellite PRN03.

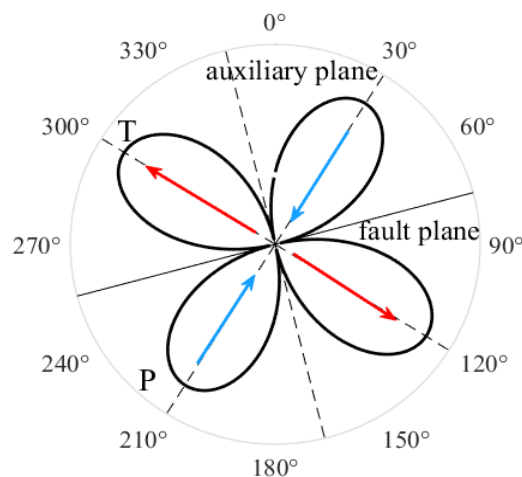
367

368 *3.4. Discussion*

369 The eruption of the 2020 Jamaica strike-slip earthquake excites seismic Rayleigh surface
 370 waves which propagate along the southwest direction (around azimuth 210°) and southeast
 371 direction (around azimuth 120°). The Rayleigh surface waves induce the secondary acoustic
 372 wave with dynamic coupling in a few kilometers away from epicenter and cause TEC
 373 fluctuation in the ionosphere height, and the distinct co-seismic ionospheric disturbances,
 374 appear and are detected by GPS observation after about 12min of the main shock. The

375 detection of distinct TEC disturbance demonstrate that the strike-slip Jamaica earthquake can
 376 also cause large amount vertical displacement [26,28], although the amount is still less than a
 377 dip-slip earthquake of the same magnitude. The maximum variation amplitude of TEC series
 378 obtained from GPS measurement reaches more than 0.1 TECU. The amplitude of TEC series
 379 decreases with the increasing distance between SIPs and epicenter. The TEC disturbances
 380 appear in the southeast near-field and southwest far-field area of the epicenter and last for
 381 less than half an hour, when combined with the TEC distribution maps in Figure 3. Satellite
 382 PRN26 and PRN03 detected two different TEC disturbances respectively during the 2020
 383 Jamaica earthquake. Furthermore, the propagation velocity, amplitude, frequency, maximum
 384 of TEC series and corresponding elevation angle and azimuth changes from the two-azimuth
 385 TEC disturbances are estimated and analyzed in above sections. We have discussed the CID
 386 source through estimating the propagation speed and frequency characteristic of the
 387 disturbance signals. Besides, the azimuthal asymmetry of CID amplitude and the detection of
 388 the inverted *N*-shape waveform in seismic ionospheric disturbance are the main differences
 389 and may reveal the deep relationship among CID, Rayleigh wave and earthquake..

390 As is mentioned in section 3.3, the disturbance signals display in the forms of inverted
 391 *N*-shape wave and typical *N*-shape wave. This demonstrates that the two-azimuth
 392 ionospheric disturbances appear in different initial polarity attribute to different
 393 ground-motion pattern. Astafyeva and Heki (2009) suggested that the waveform of
 394 disturbance signals repeat the initial ground crustal motion. The typical and inverse *N*-shape
 395 wave are caused by mixed type of focal mechanism [17]. Besides, according to Kiratzi (2014),
 396 the focal mechanism can be determined by the first motion polarity of the body and surface
 397 wave [29]. Figure 13 represents the schematic diagram for focal mechanism. The *P*-axis, *T*-axis,
 398 fault plane and auxiliary plane are labeled in the diagram. The origin represents the
 399 hypocenter and the theta axis shows the epicenter azimuth (in degree). It indicates that
 400 during the slip, the southwest quadrant is a compression region while the southeast quadrant
 401 can be considered as a dilatation or extension region. Thus, the appearance of inverted
 402 *N*-shaped wave in the southwest area detected by PRN26 attributes to the negative co-seismic
 403 vertical crustal movement, and the typical *N*-shape wave detected in the near-field southeast
 404 area ascribes to the co-seismic vertical ground uplift. This conclusion matches the Rayleigh
 405 waves shown in Figure 11(b) and (d).



407 **Figure 13.** Schematic diagram for focal mechanism.

408 However, Rolland et al (2013) argued that the amplitude and waveform of TEC signals
409 may be controlled by other factors, such as geomagnetic field, geometry of GPS-sounding and
410 background ionization. Thus, we obtained the detailed information about the geomagnetic
411 field near the epicenter area using the IGRF model from National Oceanic and Atmospheric
412 Administration (NOAA, <https://www.ngdc.noaa.gov>). The geomagnetic field has a westerly
413 declination around 6.40° , and an inclination 47.65° at the ionosphere height of 350km. It can
414 be concluded that the geomagnetic field hardly influence the amplitude and phase of CID, as
415 the Rayleigh-induced disturbance wave vector in two azimuths propagate at small angles
416 (less than 30°) to the MF line [9, 26]. Besides, no distinct TEC anomaly can be detected on the
417 north from the epicenter, which is consistent with the 'ionospheric radiation pattern' derived
418 from Rolland et al (2013).

419 As for the azimuthal asymmetry of CID amplitude, however, we have discussed the
420 factor of GPS-sounding geometry and suggested that the elevation angle is not the main
421 reason for azimuthal asymmetry of CID amplitude in section 3.2. We infer that the azimuthal
422 asymmetry of CID amplitude may attribute to the factors of vertical and horizontal crustal
423 displacements in different azimuths, even, the propagation media for CIDs. However, as the
424 absence of the TEC-time series for PRN26 during the range of 400-700km away from the
425 epicenter, further researches about the influence of horizontal and vertical crustal
426 displacement in the amplitude of CIDs are needed in the future.

427 **4. Summary**

428 In this article, the ionospheric responses following the 2020 M_w 7.7 Jamaica earthquake
429 are studied and estimated by dense GPS measurements. The co-seismic ionospheric
430 disturbances are significantly detected by Satellite PRN26 and PRN03 in two different
431 azimuths after about 12min of the main shock. The one exists in the southwest area 800km
432 away from the epicenter with the propagation velocity of 2.53km/s, while the other is
433 detected by PRN03 in the southeast area 200-450km away from the epicenter with the speed
434 of 2.57km/s. The variation amplitude of the disturbances detected by PRN26 is larger than the
435 PRN03's. The average variation amplitude of the disturbances detected by PRN26 reaches to
436 0.08 TECU, while the PRN03's reaches only to 0.05TECU. Besides, the center frequency of the
437 selected disturbances signals detected by PRN26 are about 3.4mHz and 3mHz, while the
438 disturbances signals detected by PRN03 are centered at 3.3mHz and 3.1mHz. These
439 disturbance signals all belong to infrasonic wave. Finally, by estimating the characteristic of
440 CID, the two-azimuth ionospheric disturbances are both secondary acoustic waves in the
441 infrasonic frequency range induced by the seismic Rayleigh surface wave propagating along
442 southwest direction and southeast direction with dynamic coupling.

443

444 Acknowledge:

445 This work was supported by the National Natural Science Foundation of China (NSFC)
446 Project (Grant No. 12073012) and National Natural Science Foundation of China-German

447 Science Foundation (NSFC-DFG) Project (Grant No. 41761134092). Great gratitude to
448 UNAVCO for providing the GPS observation data, IRIS seismograph data and Rayleigh wave
449 radiation pattern data (<http://www.iris.edu>) and NOAA (<http://www.ngdc.noaa.gov>) for
450 providing geomagnetic filed information.

451

452

453 **References**

454 1. Ronald V. Row. Evidence of Long-Period Acoustic-Gravity Waves Launched into the F Region by the
455 Alaskan. *Journal of Geophysical Research*, **1966**, 71(1):343-345.

456 2. Ronald V. Row. Acoustic - gravity waves in the upper atmosphere due to a nuclear detonation and
457 an earthquake. *Journal of Geophysical Research*, **1967**, 72(5):1599-1610.

458 3. R. S. Leonard, R. A. Barnes, JR. Observation of Ionospheric Disturbances Following the Alaska
459 Earthquake. *Journal of Geophysical Research*, **1965**, 70(5):1250-1253.

460 4. Davies K, Baker D M. Ionospheric effects observed around the time of the Alaskan earthquake of
461 March 28, 1964. *Journal of Geophysical Research*, **1965**, 70(9):2251-2253.

462 5. Calais, E., Minster, J. B. GPS detection of ionospheric perturbations following the January 17, 1994,
463 Northridge earthquake. *Geophysical Research Letters*, **1995**, 22(9):1045-1048.

464 6. Giovanni Occhipinti, Philippe Dorey, Thomas Farges, et al. Nostradamus: The radar that wanted to
465 be a seismometer. *Geophysical Research Letters*, **2010**, 37(18).

466 7. Jin, S. G., Wang, J., Zhang, H., and Zhu, W. Y. Real-time monitoring and prediction of the total
467 ionospheric electron content by means of GPS observations. *Chinese Astronomy and Astrophysics*, **2004**,
468 28(3):331 - 337.

469 8. Jin, S. G., Jin, R., Kutoglu, H. Positive and negative ionospheric responses to the March 2015
470 geomagnetic storm from BDS observations. *Journal of Geodesy*, **2017**, 91(6):613-626.

471 9. Rolland, L. M., Vergnolle, M., Nocquet, J. M., et al. Discriminating the tectonic and non-tectonic
472 contributions in the ionospheric signature of the 2011, Mw 7.1, dip-slip van earthquake, eastern Turkey.
473 *Geophysical Research Letters*, **2013**, 40:2518-2522.

474 10. Afraimovich E L, Ding F, Kiryushkin V V, et al. TEC response to the 2008 Wenchuan Earthquake in
475 comparison with other strong earthquakes. *International Journal of Remote Sensing*, **2010**,
476 31(13):3601-3613.

477 11. S. Sripathi, Ram Singh, Prabhakar Tiwari, et al. On the Co-Seismic Ionospheric Disturbances (CIDs)
478 in the Rapid Run Ionosonde Observations Over Allahabad Following Mw 7.8 Nepal Earthquake on
479 April 25, 2015. *Journal of Geophysical Research*, **2020**, 125(1):2169-2185.

480 12. Y. Zhou, et al., Ionospheric disturbances associated with the 2015 M7.8 Nepal earthquake, *Geodesy*
481 and *Geodynamics* (2017), <http://dx.doi.org/10.1016/j.geog.2017.04.004>

482 13. Jann-Yenq Liu, Chia-Hung Chen, Chien-Hung Lin, et al. Ionospheric disturbances triggered by the

- 483 11 March 2011 M 9.0 Tohoku earthquake. *Journal of Geophysical Research*, **2011**, 116(A6).
- 484 14. Saito, A., Tsugawa, T., Otsuka, Y., et al. Acoustic resonance and plasma depletion detected by
485 GPS total electron content observation after the 2011 off the Pacific coast of Tohoku earthquake. *Earth,*
486 *Planets and Space*, **2011**, 63(7):863-867.
- 487 15. Tsugawa T, Saito A, Otsuka Y, et al. Ionospheric disturbances detected by GPS total electron content
488 observation after the 2011 Tohoku earthquake. AGU Fall Meeting Abstracts, **2011**.
- 489 16. Perevalova, N.P., V.A. Sankov, E.I. Astafyeva, A.S. Zhupityaeva. Threshold magnitude for
490 ionospheric response to earthquakes, *J. Atmos. Solar-Terr. Physics*, **2014**, 108:77-90.
- 491 17. Astafyeva, E., Heki, K. Dependence of waveform of near-field coseismic ionospheric disturbances on
492 focal mechanisms. *Earth, Planets and Space*, **2009**, 61(7):939-943.
- 493 18. K. Heki, Y. Otsuka, N. Choosakul, N. Hemmakorn, T. Komolmis, T. Maruyama. Detection of
494 ruptures of Andaman fault segments in the 2004 Great Sumatra Earthquake with coseismic ionospheric
495 disturbances, *J. Geophys. Res.*, **2006**, 111.
- 496 19. E.L. Afraimovich, K.S. Palamartchouk, N.P. Perevalova. GPS radio interferometry of traveling
497 ionospheric disturbances. *J. Atmos. Sol.-Terr. Phys.*, **1998**, 60(12):1205-1233.
- 498 20. Brunini, C., Azpilicueta, F. J. Accuracy assessment of the GPS-based slant total electron content.
499 *Journal of Geodesy*, **2009**, 83(8):773 - 785.
- 500 21. Jin, S.G., Jin, R., Li, D. GPS detection of ionospheric Rayleigh wave and its source following the 2012
501 Haida Gwaii earthquake. *Journal of Geophysical Research*, **2017**, 122(1):1360-1372.
- 502 22. Nguyen, V.K., Rovira-Garcia, A., Juan, J.M. et al. Measuring phase scintillation at different
503 frequencies with conventional GNSS receivers operating at 1 Hz. *Journal of Geodesy*, **2019**, 93:1985-2001.
- 504 23. Cai, C., Liu, Z., Xia, P., et al. Cycle slip detection and repair for undifferenced GPS observations
505 under high ionospheric activity. *GPS Solutions*. **2013**, 17:247-260.
- 506 24. Jin, S.G. Two-mode ionospheric disturbances following the 2005 Northern California offshore
507 earthquake from GPS measurements. *Journal of Geophysical Research*, **2018**, 123:8587-8598.
- 508 25. Astafyeva, E., Heki, K., Kiryushkin, V., Afraimovich, E., and Shalimov, S. Two - mode long - distance
509 propagation of coseismic ionosphere disturbances. *J. Geophys. Res.*, **2009**, 114 (A10):307.
- 510 26. Astafyeva, E., Rolland, L.M., Sladen, A. Strike-slip earthquakes can also be detected in the
511 ionosphere. *Earth. Planet. Sci. Lett.*, **2014**, 405:180-193.
- 512 27. Astafyeva, E., Shalimov, S., Olshanskaya, E., Lognonné, P. Ionospheric response to earthquakes of
513 different magnitudes: larger quakes perturb the ionosphere stronger and longer. *Geophys. Res. Lett.*, **2013**,
514 40(9):1675-1681.
- 515 28. Mokhammad Nur Cahyadi, Kosuke Heki. Coseismic ionospheric disturbance of the large strike-slip
516 earthquakes in North Sumatra in 2012: Mw dependence of the disturbance amplitudes, *Geophysical*
517 *Journal International*, **2015**, 200(1):116-129.
- 518 29. Kiratzi, A.A. Mechanism of earthquake in Aegean. *Encyclopedia of Earthquake Engineering*, **2014**,

519 4:3966.

520